LETTER

doi:10.1038/nature24266

History-independent cyclic response of nanotwinned metals

Qingsong Pan[1]*, Haofei Zhou[2]*, Qiuhong Lu[1], Huajian Gao[2] & Lei Lu[1]

Nearly 90 per cent of service failures of metallic components and structures are caused by fatigue at cyclic stress amplitudes much lower than the tensile strength of the materials involved[1]. Metals typically suffer from large amounts of cumulative, irreversible damage to microstructure during cyclic deformation, leading to cyclic responses that are unstable (hardening or softening)[2–4] and history-dependent[5–8]. Existing rules for fatigue life prediction, such as the linear cumulative damage rule[1,9], cannot account for the effect of loading history, and engineering components are often loaded by complex cyclic stresses with variable amplitudes, mean values and frequencies[10,11], such as aircraft wings in turbulent air. It is therefore usually extremely challenging to predict cyclic behaviour and fatigue life under a realistic load spectrum[1,11]. Here, through both atomistic simulations and variable-strain-amplitude cyclic loading experiments at stress amplitudes lower than the tensile strength of the metal, we report a history-independent and stable cyclic response in bulk copper samples that contain highly oriented nanoscale twins. We demonstrate that this unusual cyclic behaviour is governed by a type of correlated 'necklace' dislocation consisting of multiple short component dislocations in adjacent twins, connected like the links of a necklace. Such dislocations are formed in the highly oriented nanotwinned structure under cyclic loading and help to maintain the stability of twin boundaries and the reversible damage, provided that the nanotwins are tilted within about 15 degrees of the loading axis. This cyclic deformation mechanism is distinct from the conventional strain localizing mechanisms associated with irreversible microstructural damage in single-crystal[12,13], coarse-grained[1,14], ultrafine-grained and nanograined metals[4,15,16].

Direct-current electrodeposition was used to prepare bulk high-purity copper plates (thickness $\geq$3 mm) with nanoscale growth twins[17,18], which were cut into dog-bone-shaped specimens for cyclic tests (Fig. 1a). Cross-sectional scanning electron microscopy (SEM) observations revealed that most grains are columnar in shape and separated by sharp grain boundaries (Fig. 1b). High-density nanoscale growth twins were detected in all grains by cross-sectional transmission electron microscopy (TEM) (Fig. 1c). Nanotwinned copper (NT-Cu) samples with average grain size $d = 5.7\,\mu\text{m}$ and twin thickness $\lambda = 63$ nm are referred to as NT-Cu-A (Fig. 1b, c) and those with larger grain size of 8.2 μm and twin thickness of 79 nm are referred to as NT-Cu-B. A strong {111} out-of-plane texture exists in as-prepared NT-Cu, because most twin boundaries (TBs) are roughly parallel to the deposition plane, as shown by the (111) pole figure derived from X-ray diffraction (Fig. 1d) and electron backscatter diffraction measurements (Supplementary Video 1). Monotonic tensile properties of both NT-Cu samples are summarized in Extended Data Fig. 1.

To explore the effect of the loading history on the cyclic response of NT-Cu, we carried out uniaxial symmetric tension–compression cyclic deformation tests at room temperature, with plastic strain amplitude $\Delta\varepsilon_{\rm pl}/2$ increasing stepwise from 0.02% to 0.04%, 0.06% and finally 0.09%, and then decreasing sequentially back to 0.02% (Extended Data Fig. 2). The loading axis is approximately parallel to the majority of the twin planes (Fig. 1). Figure 2 shows variations of the stress amplitude $\Delta\sigma/2$ versus the cumulative cycles $\sum N$ for samples NT-Cu-A (Fig. 2a, b) and NT-Cu-B (Fig. 2d, e), which were cyclically deformed in prescribed sequences of stepwise increasing and decreasing $\Delta\varepsilon_{\rm pl}/2$. Taking NT-Cu-A as an example, it is seen that $\Delta\sigma/2$ quickly reaches a steady state value of about 162 MPa at $\Delta\varepsilon_{\rm pl}/2 = 0.02\%$ and remains constant over the rest of the loading cycles, indicating a stable cyclic response. Similar cyclic stability is observed as $\Delta\varepsilon_{\rm pl}/2$ is raised stepwise up to 0.09% and then decreased back to 0.02%, with a total cumulative fatigue life exceeding 17,000 cycles. The results also revealed a one-to-one correspondence between $\Delta\sigma/2$ and $\Delta\varepsilon_{\rm pl}/2$. The value of $\Delta\sigma/2$ during the decreasing $\Delta\varepsilon_{\rm pl}/2$ sequence is nearly identical to that during the increasing sequence at the same $\Delta\varepsilon_{\rm pl}/2$, indicating a history-independent cyclic response. The larger the $\Delta\varepsilon_{\rm pl}/2$, the higher the $\Delta\sigma/2$. Similar behaviour was observed in NT-Cu-B, but with a lower stable stress level at the same $\Delta\varepsilon_{\rm pl}/2$ owing to the larger twin thickness and a longer cumulative fatigue life of up to 25,000 cycles. Even after more than 1,000% cumulative plastic strain, this stable cyclic response with one-to-one $\Delta\sigma/2$–$\Delta\varepsilon_{\rm pl}/2$ correspondence still persists in both NT-Cu samples (Extended Data Fig. 3a–d).

The stress–strain hysteresis loops of NT-Cu at a given strain amplitude during the increasing/decreasing $\Delta\varepsilon_{\rm pl}/2$ sequences are also identical, as shown in Fig. 2c and f. In particular, for each $\Delta\varepsilon_{\rm pl}/2$, both the ascending and descending branches of the hysteresis loops in the decreasing $\Delta\varepsilon_{\rm pl}/2$ sequence overlap completely with those in the increasing $\Delta\varepsilon_{\rm pl}/2$ sequence. Irrespective of the imposed $\Delta\varepsilon_{\rm pl}/2$ and the loading sequence (ascending or descending), they all obey the same stress–strain response.

Symmetric tension–compression cyclic tests with stepwise increasing and decreasing $\Delta\varepsilon_{\rm pl}/2$ were also performed on NT-Cu, ultrafine-grained Cu (UFG-Cu) and coarse-grained Cu (CG-Cu) samples at larger $\Delta\varepsilon_{\rm pl}/2$ from 0.05% to 0.25% with 70 loading cycles at each $\Delta\varepsilon_{\rm pl}/2$ value (Extended Data Fig. 3e–m). Conventional history-dependent cyclic responses were observed in CG-Cu and UFG-Cu, as reported in the literature[4,5,8]. These results clearly indicate that the NT-Cu samples exhibit a unique, stable and history-independent cyclic response during cyclic deformation, irrespective of the imposed plastic strain amplitudes and cycle numbers.

To understand the underlying deformation mechanisms of the history-independent and stable cyclic response, we performed large-scale atomistic simulations of NT-Cu similar to the experimental setup (see Methods and Extended Data Figs 4 and 5). Figure 3a and b provides two different cross-sectional views of a deformed grain (marked as G1 in Extended Data Fig. 4) in the simulated NT-Cu sample after 20 cycles at $\Delta\varepsilon_{\rm pl}/2 = 0.25\%$. It is seen that dislocations that carry plastic deformation in NT-Cu during cyclic loading are strongly correlated across multiple TBs, with a necklace-like structure. These correlated necklace

---

[1]Shenyang National Laboratory for Materials Science, Institute of Metal Research, Chinese Academy of Sciences, Shenyang 110016, China. [2]School of Engineering, Brown University, Providence, Rhode Island 02912, USA.
*These authors contributed equally to this work.

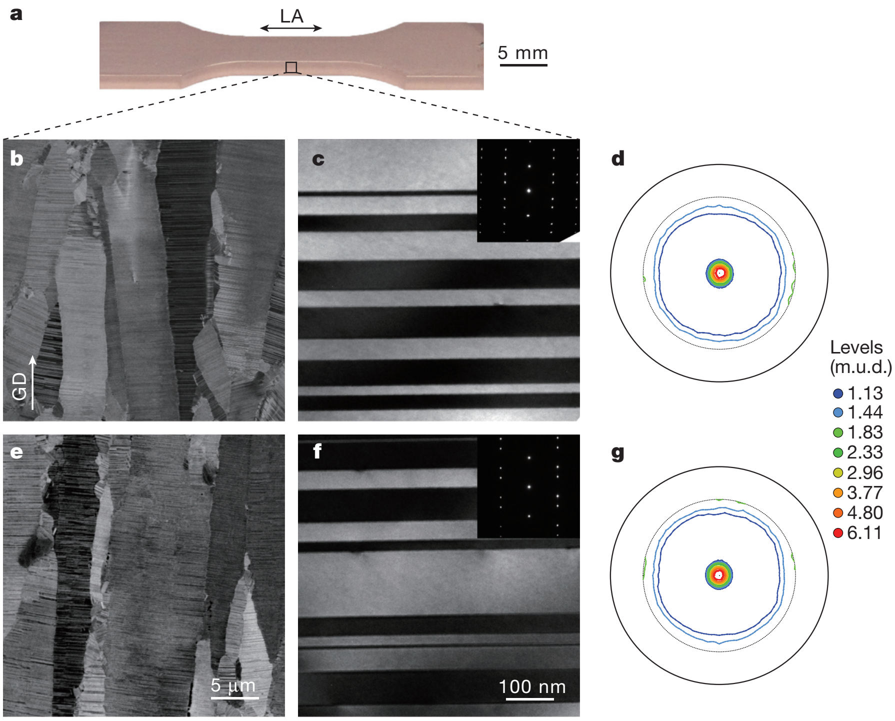

Figure 1 | Microstructure of NT-Cu before and after cyclic deformation. **a**, Image of an as-deposited NT-Cu-A specimen for cyclic loading tests. **b**–**g**, Cross-sectional SEM (**b**) and TEM (**c**) and plane-view X-ray diffraction observations (**d**) showing that the sample contains a high density of parallel nanoscale twins in micrometre-sized columnar grains, and that the microstructure is preserved (**e**, **f**, **g**) even after a cumulative life of 17,000 loading cycles. Insets in **c** and **f** show selected area diffraction patterns of nanoscale twins. GD stands for the growth direction and LA indicates the cyclic loading axis, which is approximately parallel to the twin planes. Levels (m.u.d., multiples of uniform density) denote the intensity of texture.

dislocations (CNDs) are identified as a new type of dislocation structure which is fundamentally distinct from typical dislocation patterns observed in conventional single-crystal[13] and coarse-grained metals[1,14] during fatigue, as well as in dislocations that pile up at TBs[19], twinning partials[20–24] and threading dislocation[17] in nanotwinned metals during monotonic tensile tests. During the simulation, CNDs were observed to move collectively back and forth along the TBs under cyclic loading (Supplementary Videos 2 and 3). The observed CND structure is consistent with experimentally observed zigzag deformation patterns at the surface of the NT-Cu samples after cyclic testing (Fig. 3c).

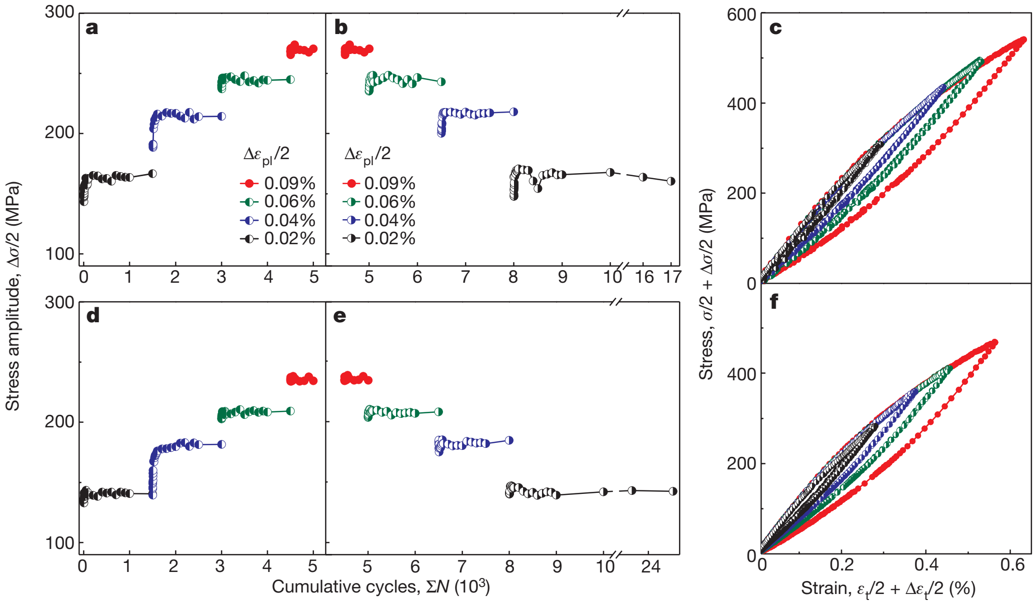

Figure 2 | History-independent cyclic deformation behaviour of NT-Cu. **a**, **b**, **d**, **e**, Cyclic stress response $\Delta\sigma/2$ as a function of the cumulative loading cycles $\sum N$ for NT-Cu-A (**a**, **b**) and NT-Cu-B (**d**, **e**) samples cyclically deformed in two sequences of plastic strain amplitudes, that is, increasing $\Delta\varepsilon_{\mathrm{pl}}/2$ step-by-step from 0.02% to 0.09% (**a**, **d**) and decreasing $\Delta\varepsilon_{\mathrm{pl}}/2$ back to 0.02% (**b**, **e**). **c**, **f**, The corresponding hysteresis loops (at the 500th cycle at each $\Delta\varepsilon_{\mathrm{pl}}/2$) for NT-Cu-A (**c**) and NT-Cu-B (**f**) samples in a shifted coordinate system, where the lower left corners of the loops are shifted to the coordinate origin for comparison purposes. More than 10 individual nanotwinned samples were tested, each being 49 mm in total length and 12 mm × 4 mm × 3.2 mm in the gauge section.

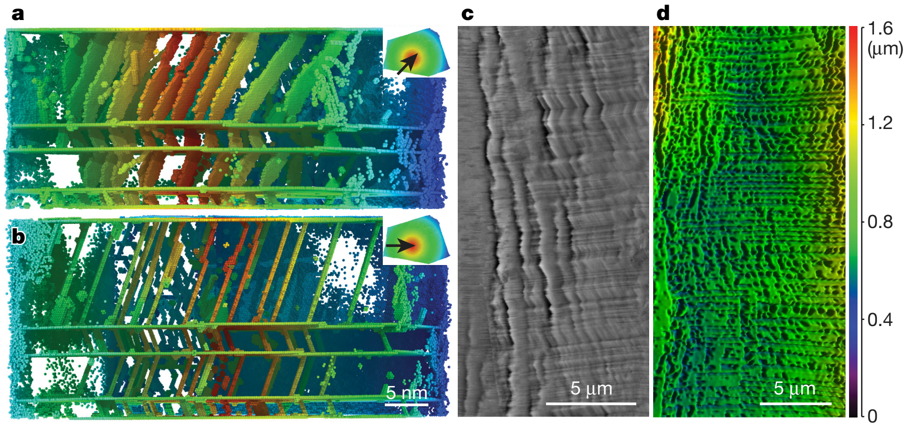

Figure 3 | Cyclic deformation features of NT-Cu. a, **b**, Simulated cyclic deformation patterns of CNDs in grain G1 (see Extended Data Fig. 4) after 20 cycles. The insets show the top view of the grain of interest, with arrows indicating the viewing angles. Atoms in the face-centred-cubic (fcc) structure are made transparent for clarity. Colours are assigned to atoms according to their spatial coordinates. **c**, **d**, Cross-sectional SEM (**c**) and confocal laser scanning microscopy observations (**d**) of NT-Cu-A after cyclic loading, showing zigzag slip bands across TBs (**c**) with very little height fluctuation (**d**). The contrast in **d** indicates height fluctuation as shown by the colour bar on the right.

The slip patterns cut through numerous TBs, with lengths ranging from several to tens of micrometres, and lay parallel to each other while being inclined to TBs in individual twin interiors, implying that only a single slip system with slip plane inclined to TBs was active during the cyclic tests (Fig. 3a, b). Confocal laser scanning microscopy observations in Fig. 3d showed that the mean surface height fluctuation associated with the slip patterns, defined as the altitude difference between adjacent surface peaks and troughs, was only 310 nm in NT-Cu-A when the sample was cycled to failure, which is much smaller than typical micrometre-scale extrusions or intrusions associated with strain localization in fatigued single-crystal and coarse-grained metals[1,14].

To examine the microstructure underneath the zigzag slip bands, the top surface of NT-Cu-A after 17,000 cycles of deformation was mechanically polished. No detectable changes in TB morphologies, TB spacing, grain size and texture were found between the as-deposited state and those during and after cyclic deformation (Fig. 1, Extended Data Fig. 6 and Supplementary Video 1), indicating an extremely stable microstructure under variable cyclic loading.

Based on the double Thompson tetrahedron for twin and matrix[25], we found that the CND is made up of a series of single-slip threading dislocation segments gliding on inclined slip planes between adjacent TBs, as well as twinning partial dislocations lying on TBs, and stair-rod dislocations at the intersection of the inclined slip planes and twin planes (Extended Data Fig. 7a–d). Most CNDs are formed by linking neighbouring threading dislocations through dissociation and merging of their misfit tails on TBs under cyclic loading (Extended Data Fig. 7e–h), which is different from that of jogged CNDs[26] found in simulated nanotwinned metal with $\lambda < 1$ nm under monotonic loading. The highly correlated CNDs provide an interesting mechanism for carrying plastic strain in neighbouring twin/matrix lamellae without any strain localization (Fig. 3d) and also seem capable of hindering the formation of dislocation locks or entanglements (Extended Data Fig. 8). More importantly, the extremely stable CND structure moving back and forth along the TBs during cyclic deformation preserves the slip system as well as the coherency and stability of TBs (Fig. 1e, f, Supplementary Video 1). Our simulations also demonstrated that history-independent cyclic behaviour is an inherent property of the highly oriented nanotwinned structure, provided that the TBs are tilted within about 15° relative to the loading axis (Extended Data Fig. 9 and Supplementary Videos 5–8).

A two-beam diffraction technique in TEM[27] was adopted to characterize the configurations of CNDs in the twin/matrix lamellae of cyclically deformed NT-Cu-A (Fig. 4a, b). Three-dimensional stereo-projection reconstructions of CNDs and nanoscale twins under a viewing direction inclined to TBs are shown in Fig. 4c, where the twin planes are projected as regions of moiré fringes. Owing to the severe confinement of nanoscale twins, the overall morphology of CNDs with curved heads cannot easily be observed by TEM. Only their relatively long segments overlapping with TBs can be detected in nanometre-thick TEM foils, as schematically illustrated by the solid lines in Fig. 4c. Short, parallel dislocation segments overlapping with moiré fringes were prevalently detected in some grains (Fig. 4a), which is fully consistent with the anticipated structure of CNDs (Fig. 4c). The visible dislocation segments under diffraction vectors $\boldsymbol{g} = [\bar{2}00]_{\mathrm{M}}$ (Fig. 4b) and $[\bar{1}11]_{\mathrm{M}}$ from the matrix (or $[\bar{2}00]_{\mathrm{T}}$ and $[\bar{1}11]_{\mathrm{T}}$ from the twin) suggest that their Burgers vectors are parallel to TBs[28] (Extended Data Table 1). The distribution of dislocation segments is not random, but uniform with nearly identical spacing, suggesting that they are highly correlated (see the black dot-dashed line in Fig. 4a). These analyses based on SEM, TEM and three-dimensional stereo-projection reconstruction thus collectively support the idea that the observed dislocation segments on TBs correspond to the CNDs observed in atomistic simulations.

The observed history-independent and stable cyclic response governed by mobile, single-slip and extremely stable CNDs reveals a new route to the design of engineering structures that are resistant to fatigue and damage accumulation, by using highly oriented nanotwinned

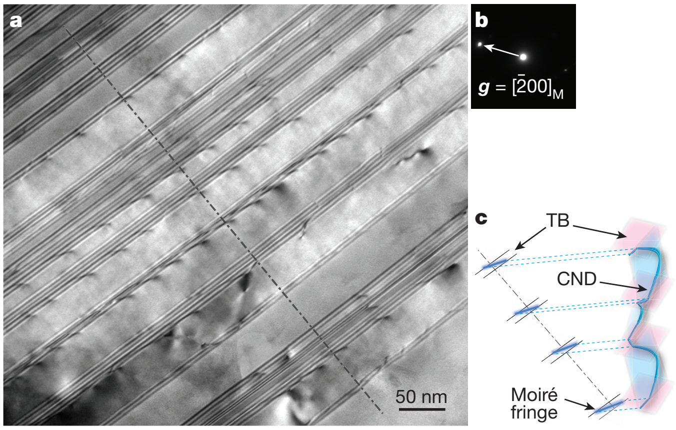

Figure 4 | CND morphology in cyclically deformed NT-Cu. a, Cross-sectional TEM images of cyclically deformed NT-Cu-A showing that typical segments of CNDs overlapping with moiré fringes of TBs are uniformly distributed. **b**, The diffraction vector $\boldsymbol{g} = [\bar{2}00]_{\mathrm{M}}$. **c**, Schematic of CNDs in adjacent twins under two-beam conditions, with blue solid lines marking the CND segments overlapping with TBs.

metals that have been synthesized by various growth and deformation processing techniques[29–32].

Online Content Methods, along with any additional Extended Data display items and Source Data, are available in the online version of the paper; references unique to these sections appear only in the online paper.

Received 26 June 2016; accepted 15 August 2017.

1. Suresh, S. *Fatigue of Materials* 2nd edn (Cambridge Univ. Press, 1998).
2. Smith, R. W., Hirschberg, M. H. & Manson, S. S. *Fatigue Behavior of Materials under Strain Cycling in Low and Intermediate Life Range* (NASA, 1963).
3. Polakowski, N. H. Softening of cold-worked metals under cyclic strains. *Nature* **171,** 173 (1953).
4. Mughrabi, H. & Höppel, H. W. Cyclic deformation and fatigue properties of very fine-grained metals and alloys. *Int. J. Fatigue* **32,** 1413–1427 (2010).
5. Feltner, C. E. & Laird, C. Cyclic stress–strain response of FCC metals and alloys 1. Phenomenological experiments. *Acta Metall.* **15,** 1621–1632 (1967).
6. Laird, C., Finney, J. M., Schwartzman, A. & Veaux, R. D. L. History dependence in cyclic stress-strain response of wavy slip materials. *J. Test. Eval.* **3,** 435–441 (1975).
7. Mecke, K. TEM investigations of cyclic stress strain behavior and formation of persistent slip bands in fatigued single-crystals of nickel using changing amplitude tests. *Phys. Status Solidi A* **25,** K93–K96 (1974).
8. Lukáš, P. & Klesnil, M. Cyclic stress–strain response and fatigued life of metals in low amplitude region. *Mater. Sci. Eng.* **11,** 345–356 (1973).
9. May, A. N. Fatigue under random loads. *Nature* **192,** 158–159 (1961).
10. Head, A. K. & Hooke, F. H. Fatigue of metals under random loads. *Nature* **177,** 1176–1177 (1956).
11. Schijve, J. *Fatigue of Structures and Materials* 2nd edn (Springer, 2009).
12. Mughrabi, H. Cyclic hardening and saturation behavior of copper single-crystals. *Mater. Sci. Eng.* **33,** 207–223 (1978).
13. Li, P., Li, S. X., Wang, Z. G. & Zhang, Z. F. Fundamental factors on formation mechanism of dislocation arrangements in cyclically deformed fcc single crystals. *Prog. Mater. Sci.* **56,** 328–377 (2011).
14. Peralta, P. & Laird, C. in *Physical Metallurgy* 5th edn (eds Laughlin, D. E. & Hono, K.) 1765–1880 (Elsevier, 2014).
15. Hanlon, T., Kwon, Y. N. & Suresh, S. Grain size effects on the fatigue response of nanocrystalline metals. *Scr. Mater.* **49,** 675–680 (2003).
16. Pineau, A., Amine Benzerga, A. & Pardoen, T. Failure of metals III. Fracture and fatigue of nanostructured metallic materials. *Acta Mater.* **107,** 508–544 (2016).
17. You, Z. S., Lu, L. & Lu, K. Tensile behavior of columnar grained Cu with preferentially oriented nanoscale twins. *Acta Mater.* **59,** 6927–6937 (2011).
18. Pan, Q. S. & Lu, L. Strain-controlled cyclic stability and properties of Cu with highly oriented nanoscale twins. *Acta Mater.* **81,** 248–257 (2014).
19. Lu, K., Lu, L. & Suresh, S. Strengthening materials by engineering coherent internal boundaries at the nanoscale. *Science* **324,** 349–352 (2009).
20. Wang, J. *et al.* Detwinning mechanisms for growth twins in face-centered cubic metals. *Acta Mater.* **58,** 2262–2270 (2010).
21. Shute, C. J. *et al.* Detwinning, damage and crack initiation during cyclic loading of Cu samples containing aligned nanotwins. *Acta Mater.* **59,** 4569–4577 (2011).
22. Yoo, B.-G. *et al.* Quantitative damage and detwinning analysis of nanotwinned copper foil under cyclic loading. *Acta Mater.* **81,** 184–193 (2014).
23. Wang, Y. M. *et al.* Defective twin boundaries in nanotwinned metals. *Nat. Mater.* **12,** 697–702 (2013).
24. Jang, D. C., Li, X. Y., Gao, H. J. & Greer, J. R. Deformation mechanisms in nanotwinned metal nanopillars. *Nat. Nanotech.* **7,** 594–601 (2012).
25. Zhu, T. & Gao, H. J. Plastic deformation mechanism in nanotwinned metals: an insight from molecular dynamics and mechanistic modeling. *Scr. Mater.* **66,** 843–848 (2012).
26. Zhou, H. F., Li, X. Y., Qu, S. X., Yang, W. & Gao, H. J. A jogged dislocation governed strengthening mechanism in nanotwinned metals. *Nano Lett.* **14,** 5075–5080 (2014).
27. Williams, D. B. & Carter, C. B. *Transmission Electron Microscopy: A Textbook for Materials Science* 2nd edn (Springer Science/Business Media, 2009).
28. Lu, Q. H., You, Z. S., Huang, X., Hansen, N. & Lu, L. Dependence of dislocation structure on orientation and slip systems in highly oriented nanotwinned Cu. *Acta Mater.* **127,** 85–97 (2017).
29. Bufford, D. C., Wang, Y. M., Liu, Y. & Lu, L. Synthesis and microstructure of electrodeposited and sputtered nanotwinned face-centered-cubic metals. *MRS Bull.* **41,** 286–291 (2016).
30. Hodge, A. M., Wang, Y. M. & Barbee, T. W. Mechanical deformation of high-purity sputter-deposited nano-twinned copper. *Scr. Mater.* **59,** 163–166 (2008).
31. Zhang, X. *et al.* High-strength sputter-deposited Cu foils with preferred orientation of nanoscale growth twins. *Appl. Phys. Lett.* **88,** 173116 (2006).
32. Li, Y. S., Tao, N. R. & Lu, K. Microstructural evolution and nanostructure formation in copper during dynamic plastic deformation at cryogenic temperatures. *Acta Mater.* **56,** 230–241 (2008).

Supplementary Information is available in the online version of the paper.

Acknowledgements L.L. acknowledges support by the National Natural Science Foundation of China (NSFC) (grant numbers 51371171, 51471172 and U1608257) and the Key Research Program of Frontier Science, Chinese Academy of Sciences. H.G. acknowledges support by the US National Science Foundation through grant DMR-1709318. L.L. and H.G. acknowledge support by an international collaboration grant from NSFC (51420105001). The simulations reported were performed on resources provided by the Extreme Science and Engineering Discovery Environment (XSEDE) through grant MS090046. We thank H. Mughrabi for discussions and S. Jin for sample preparation.

Author Contributions L.L. and H.G. designed and supervised the project; Q.P., Q.L. and L.L. performed the experiments; H.Z. performed the atomistic simulations; Q.P., H.Z., H.G. and L.L. analysed data, developed models, discussed the results and wrote the paper.

Author Information Reprints and permissions information is available at www.nature.com/reprints. The authors declare no competing financial interests. Readers are welcome to comment on the online version of the paper. Publisher's note: Springer Nature remains neutral with regard to jurisdictional claims in published maps and institutional affiliations. Correspondence and requests for materials should be addressed to H.G. (huajian_gao@brown.edu) or L.L. (llu@imr.ac.cn).

Reviewer Information *Nature* thanks J. Wang and the other anonymous reviewer(s) for their contribution to the peer review of this work.

METHODS

Materials. High-purity copper sheets containing nanoscale growth twins were synthesized by means of a direct-current electrodeposition technique[17,18] from an electrolyte of $CuSO_4$ with concentration of 90 g l^{-1} and pH value adjusted to approximately 1 with H_2SO_4, a soluble anode made of a highly purified (99.995 wt%) electrolytic copper sheet, and a pure Ti sheet as cathode substrate. The distance between the anode and cathode was approximately 10 cm. The electrolyte bath was stirred mechanically and the bath temperature was set at 20 °C. NT-Cu samples with different grain sizes and twin thicknesses were prepared by adjusting the current density. As-deposited NT-Cu samples exhibit the following approximate dimensions: length 50 mm, width 40 mm and thickness 3.4 mm (Supplementary Video 1)

For comparison, high-purity twin-free UFG-Cu samples with an average grain size of about 380 nm were produced by cold-rolling CG-Cu samples with a rolling strain $\varepsilon = (t_0 - t)/t = 450\%$, where t_0 and t denote the thickness of the initial and as-rolled samples, respectively. CG-Cu samples with an average grain size of about 9.8 μm, having grain size comparable to that of NT-Cu but no notable density of twins, were produced by annealing the cold-rolled UFG-Cu samples at 250 °C for 2 h in air. Other details of sample preparation procedures can be found in ref. 18.

Uniaxial tensile properties. Uniaxial tensile tests of NT-Cu, UFG-Cu and CG-Cu were performed at strain rate of 2×10^{-3} s^{-1}. Tensile tests reveal that NT-Cu-A displays a yield strength (σ_y) of 328 MPa and an ultimate tensile strength (σ_{uts}) of 379 MPa, comparable to that ($\sigma_y = \sigma_{uts} \approx 370$ MPa) of twin-free UFG-Cu. NT-Cu-B exhibits a lower strength, owing to wider twin thickness, albeit still much larger than that ($\sigma_y \approx 85$ MPa, $\sigma_{uts} \approx 231$ MPa) of twin-free CG-Cu (Extended Data Fig. 1). Although NT-Cu and UFG-Cu have comparable yield strength, cyclic softening occurs in UFG-Cu whereas NT-Cu exhibits cyclic stability (Fig. 2 and Extended Data Fig. 3).

Tension–compression cyclic tests. Dog-bone-shaped specimens with a total length of 49 mm and a gauge length of 12 mm were cut from NT-Cu, UFG-Cu and CG-Cu sheets by using an electrical spark machine. After mechanical grinding and electropolishing, the final dimensions of the gauge cross-section area of NT-Cu samples are 4 ± 0.15 mm in width and 3.2 ± 0.1 mm in thickness (Supplementary Video 1). Uniaxial cyclic tests with tension–compression symmetry and plastic strain control were performed on an Instron 8874 testing machine at ambient temperature in air. A dynamic strain-gauge extensometer (Instron Catalogue no. 2620–603) with a gauge length of 10 mm was clamped on the specimen surface by high-strength rubber bands for accurate direct measurement and closed-loop control of cyclic strain amplitude. The strain resolution and control precision are smaller than 10^{-4}. Under strain control, a triangular wave loading profile with a cyclic plastic strain rate of 1.0×10^{-3} s^{-1} was used. The applied uniaxial plastic strain amplitudes were $\Delta\varepsilon_{pl}/2 = 0.02\%$, 0.04%, 0.06% and 0.09%. Two loading sequences, that is, step-by-step increasing $\Delta\varepsilon_{pl}/2$ from 0.02% to 0.09% first and then decreasing back to 0.02%, were imposed on the NT-Cu samples (Extended Data Fig. 2). In the increasing $\Delta\varepsilon_{pl}/2$ sequence, the sample was subjected to 1,500 cycles of tension–compression loading at $\Delta\varepsilon_{pl}/2 = 0.02\%$, 0.04% and 0.06%, whereas at the maximum $\Delta\varepsilon_{pl}/2 = 0.09\%$, the number of cycles was 500. In the decreasing $\Delta\varepsilon_{pl}/2$ sequence, 1,500 cycles were imposed at $\Delta\varepsilon_{pl}/2 = 0.06\%$ and 0.04%, respectively. The sample was then cycled to failure at $\Delta\varepsilon_{pl}/2 = 0.02\%$. During the stepwise loading, the next level of plastic strain amplitude was imposed after the sample cyclically deformed at the previous strain amplitude was interrupted at the planned cycle of loading and then fully unloaded. Similar cyclic deformation tests with two sequences of stepwise increasing and decreasing $\Delta\varepsilon_{pl}/2$ from 0.05% to 0.25% were performed on NT-Cu, CG-Cu and UFG-Cu samples (Extended Data Fig. 3). More than 10 individual nanotwinned samples were cyclically deformed.

Images of the original sample, microstructure and texture evolution of NT-Cu before, during and after cyclic deformation were taken at four different stages of the cyclic loading test (see Supplementary Video 1): (1) before cycling (as-deposited sample); (2) after cyclically deforming at $\Delta\varepsilon_{pl}/2 = 0.06\%$ in the increasing $\Delta\varepsilon_{pl}/2$ sequence; (3) after cyclically deforming at $\Delta\varepsilon_{pl}/2 = 0.06\%$ in the decreasing $\Delta\varepsilon_{pl}/2$ sequence; (4) after cyclically deforming at $\Delta\varepsilon_{pl}/2 = 0.02\%$ and before failure in the decreasing $\Delta\varepsilon_{pl}/2$ sequence. Cyclic tests of NT-Cu-A samples ($d = 6.1$ μm and $\lambda = 64$ nm) were interrupted at different stages to take these images.

Microstructure observation. The cross-sectional microstructures of the NT-Cu specimens before and after cyclic deformation were examined by a field emission gun (FEI Nova NanoSEM 430) with backscattered electron imaging using a low-kilovolt, high-contrast (vCD) detector. The samples were mechanically polished, followed by electropolishing in a solution of phosphoric acid (25%), alcohol (25%) and deionized water (50%) at room temperature. The textures of the NT-Cu specimens before and after cyclic tests were examined by means of a Bruker D8 Discover X-ray diffractometer and electron backscatter diffraction on the sample surface perpendicular to the direction of deposition at room temperature. Three-dimensional slip morphologies of NT-Cu specimens after cyclic deformation were characterized by confocal laser scanning microscopy (Olympus LEXT OLS4000) with planar resolution of 120 nm and height resolution (along the z axis) of 10 nm.

Examinations of cross-sectional microstructures of NT-Cu specimens before and after cyclic deformation were also performed using an FEI Tecnai F20 TEM operated at 200 kV. A two-beam diffraction technique in TEM[27] was used to accurately characterize the Burgers vector of dislocations in twin interiors. Cross-sectional TEM foils were sliced parallel to the loading axis by electrical spark machine and mechanically polished to a final thickness of about 40 μm, and then thinned by twin-jet polishing in an electrolyte of phosphoric acid (25%), alcohol (25%) and deionized water (50%) at about −10 °C.

Cyclic response of UFG-Cu and CG-Cu. Cyclic softening was observed in UFG-Cu (Extended Data Fig. 3h, i), similar to previous reports in the literature[33,34]. As the imposed $\Delta\varepsilon_{pl}/2$ was increased from 0.05% to 0.25%, $\Delta\sigma/2$ decreased considerably. For example, $\Delta\sigma/2$ dropped rapidly at the 70th cycle of $\Delta\varepsilon_{pl}/2 = 0.05\%$, and it decreased again after cyclic deformation at $\Delta\varepsilon_{pl}/2 = 0.25\%$ for 70 cycles. Cyclic softening was also observed as $\Delta\varepsilon_{pl}$ /2 was further reduced from 0.25% to 0.05%. The history-dependent cyclic response of UFG-Cu led to a much lower $\Delta\sigma/2$ owing to the accumulated damage.

Extended Data Fig. 3k, l shows that CG-Cu exhibits history-dependent cyclic hardening behaviour[35–39], which is consistent with typical cyclic responses of single crystal and CG metals[5–8].

The evolution of the stress–strain hysteresis loop with increasing cycles is essential to understanding the nature of the cyclic response of metals[1]. The hysteresis loops of UFG-Cu in Extended Data Fig. 3j indicate that, as the cyclic test continues, the slope of the ascending branch of the hysteresis loop gradually decreases. For the hysteresis loops of CG-Cu in Extended Data Fig. 3m, the ascending branch first increases as $\Delta\varepsilon_{pl}/2$ increases from 0.05% to 0.25%, and then decreases as $\Delta\varepsilon_{pl}/2$ decreases from 0.25% to 0.05%. These history-dependent cyclic responses of UFG and CG metals are consistent with previous reports in the literature[4,40,41].

Atomistic simulations. The simulated NT-Cu sample consists of four columnar-shaped grains with a mean grain size of 40 nm (Extended Data Fig. 4a). Each grain has four subgrain twin layers with thicknesses of 12 nm, 3 nm, 5 nm and 2 nm (Extended Data Fig. 4b). This is adopted to mimic the non-uniform distribution of TBs in experiments. The system contains 12.5 million atoms. The sample is $[1\bar{1}\bar{1}]$ -textured and the four grains have in-plane orientations of 1°, 27°, 47° and 89° relative to the y axis, respectively, so that all grain boundaries are of the high-angle type (Extended Data Fig. 4c).

The system is initially equilibrated for 300 ps at 300 K, followed by a uniaxial tensile loading along the y axis to a total strain of 15%. The system is then unloaded to zero stress and equilibrated for another 200 ps. The goal is to create an initial dislocation density (approximately 12×10^{16} m^{-2}) in the system before cyclic tests. The corresponding tensile stress–strain curve is shown in Extended Data Fig. 4d. A three-step uniaxial symmetric tension–compression loading is then applied along the y axis at a constant strain rate of 1×10^9 s^{-1} (Extended Data Fig. 5a).

Throughout the simulation, periodic boundary conditions are applied in all three directions. Constant temperature and zero pressure in the non-stretching directions (that is, x axis and z axis) are controlled by a Nosé–Hoover thermostat and barostat[42,43]. The embedded-atom method potential is used to compute the interatomic forces[44]. The integration time-step is fixed at 1 fs. Two different methods are used to visualize and identify defects that emerge during plastic deformation[45]. One is based on the common-neighbour analysis[46], which leads to the following colouring scheme: grey for fcc atoms, blue for hexagonal close-packed (hcp) atoms in TBs or stacking faults, green for atoms in dislocation cores or grain boundaries. The second method is a position-based colouring scheme in which colours are assigned according to the spatial coordinates of atoms.

Simulated history-independent cyclic response. A three-step cyclic loading scheme was adopted (Extended Data Fig. 5a). The sample was loaded for six cycles at a total strain amplitude of $\Delta\varepsilon_t/2 = 1\%$, six cycles at the increased $\Delta\varepsilon_t/2 = 1.5\%$, and another six cycles as $\Delta\varepsilon_t/2$ dropped back to 1%. Extended Data Fig. 5b shows the simulated relation between stress amplitude $\Delta\sigma/2$ and cycle number N for NT-Cu. It is seen that, after six cycles as $\Delta\varepsilon_t/2$ is raised to 1.5% and another six cycles after it dropped back to $\Delta\varepsilon_t/2 = 1\%$, the measured $\Delta\sigma/2$ of NT-Cu is almost identical to that measured during the first six cycles at $\Delta\varepsilon_t/2 = 1\%$, corresponding to $\Delta\varepsilon_{pl}/2 = 0.25\%$. The ascending branches of corresponding hysteresis loops in different loading steps overlap (Extended Data Fig. 5c), similar to what is observed in Fig. 2 and Extended Data Fig. 3. It is observed that the atomic configuration of CNDs in NT-Cu exhibits extreme stability under cyclic loading (Extended Data Fig. 5d–f), with well-preserved coherent TBs (see Supplementary Videos 2 and 3). Thus, both our experiments and molecular dynamics (MD) simulations demonstrate a stable and history-independent cyclic response in NT-Cu that is not seen in CG-Cu and UFG-Cu[1,4].

Burgers vector analysis. A Burgers vector analysis of CNDs is provided in Extended Data Fig. 7a–d based on the convention of a double Thompson tetrahedron[25]. A single CND is made up of two types of dislocation segment. One type consists of several single-slip threading dislocation segments gliding on inclined slip planes between adjacent TBs, each of which is split into a leading partial, an intrinsic stacking fault, and a trailing partial. These threading dislocation segments exhibit the same Burgers vector parallel to TBs, such as $\boldsymbol{CB}$ or $\boldsymbol{C}^{\mathrm{T}}\boldsymbol{A}^{\mathrm{T}}$. The other type consists of several pairs of twinning partial dislocations lying on TBs, such as $\boldsymbol{\delta B}$ and $\boldsymbol{C\delta}$, highlighted by black triangles in Extended Data Fig. 7b–d. The above two types of dislocation segments are connected by stair-rod dislocations (such as $\boldsymbol{\alpha\delta}$) at the intersection of the inclined slip planes (such as BCD) and twin planes (ABC).

Formation of CNDs. Consider two threading dislocations of the same type (such as $\boldsymbol{CB}$) in neighbouring twin/matrix (Extended Data Fig. 7e). Owing to the confinement of nanoscale twins, each threading dislocation has two misfit tails on TBs, which can easily cross-slip onto the TBs and split into a pair of twinning partial dislocations ($\boldsymbol{\delta B}$ and $\boldsymbol{C\delta}$) (Extended Data Fig. 7f). As shown in Extended Data Fig. 7g, the two tails on the TB, one coming from the twin and the other from the matrix, have the same Burgers vector $\boldsymbol{CB}$ but opposite line directions. They can merge into a single tail in the presence of an attractive force between them under cyclic strain. This leads to the final linkage of the neighbouring threading dislocations via their misfit tails on TBs (Extended Data Fig. 7h). A statistical analysis of MD simulation results shows that CNDs formed through such a tail-linkage mechanism form the majority of the total CND density in cyclically deformed NT-Cu (Extended Data Fig. 5g). Occasionally, threading dislocations are observed to slip directly across a TB into adjacent twin layer, forming CNDs with a slightly different structure (Extended Data Fig. 7i–k). However, such direct cross-slip tends to occur under very high stress and very small TB spacing (less than 1 nm)[26] or near a sharp source such as a crack tip[47]. It is found that CNDs associated with direct cross-slip account for less than 20% of the total CND density in cyclically deformed NT-Cu. The formation mechanism of CNDs by linking misfit tails of threading dislocations is unique to cyclic loading and eliminates the constraint of very small TB spacing or availability of sharp sources[26,47,48].

Single slip versus double slip. Deformation patterns of four grains in cyclically deformed NT-Cu are shown in Extended Data Fig. 8a–d. It is seen that CNDs are dominant in G1 with a single slip system activated during cyclic deformation, leading to the formation of zigzag slip traces on the cross-section surface. On the other hand, dislocation motion along TBs is highly suppressed in G2–G4 owing to competition between two intersecting slip systems in these grains (Supplementary Video 4). Extended Data Fig. 8e and f shows x–y projection views of dislocation structures in G1 and G4, respectively. In G1, only one slip system is activated during cyclic loading, and slip traces are parallel to each other. In G4, numerous dislocation locks are formed by the operation of double slip systems, thus substantially hindering subsequent dislocation activities.

Once cyclic loading simulation begins, separate threading dislocations start to correlate with each other, forming CNDs that extend over multiple TBs. As the cyclic loading proceeds, CNDs formed in the grain periphery are absorbed by surrounding grain boundaries while those in the interior move back and forth in a reversible and stable manner, giving rise to a steady CND density in NT-Cu at a given strain amplitude (Extended Data Fig. 5h). On increasing the strain amplitude, CNDs are observed to emerge from grain boundaries as single units. Extended Data Fig. 8g–i shows snapshots of a CND emerging from a grain boundary as a single unit in cyclically deformed NT-Cu as $\Delta\varepsilon_t/2$ increases from 1% to 1.5%. This CND was absorbed by the grain boundary at $\Delta\varepsilon_t/2 = 1\%$ (Extended Data Fig. 8g) and re-emerged from the grain boundary at $\Delta\varepsilon_t/2 = 1.5\%$ (Extended Data Fig. 8h, i). Relative to the immobile dislocation locks/tangles in G2-G4, the mobile CNDs in G1 dominantly carry plastic strain in NT-Cu during cyclic loading.

Cyclic deformation of NT-Cu with TBs tilted relative to the loading direction. To explore the generality and robustness of our findings, we have further performed MD simulations on NT-Cu samples with nanotwins tilted at 5°, 10° and 15° relative to the loading direction. Extended Data Fig. 9a shows the initial configuration of a typical NT-Cu sample containing tilted TBs with respect to the loading direction. The grain size is 40 nm, and TB spacing is non-uniform with an average value of 5 nm. Each sample contains a total of 12 million atoms. The cyclic deformation patterns of NT-Cu samples with three different tilt angles of 5°, 10° and 15° are shown in Extended Data Fig. 9b, c and d, respectively. CNDs are observed in all three samples. Extended Data Fig. 9e shows typical configuration of a CND spanning across multiple tilted TBs. The threading dislocations confined in adjacent twin interiors are correlated via their tails on the tilted TBs (see black arrows in Extended Data Fig. 9e). Supplementary Videos 5–7 show cyclic deformation of NT-Cu samples containing tilted TBs at $\Delta\varepsilon_t/2 = 1.3\%$.

Extended Data Fig. 9f shows the variation of stress amplitude with the cycle number for the NT-Cu sample with a TB tilt angle of 15° during the three-step cyclic deformation process, the result indicating a stable cyclic behaviour similar to that observed in NT-Cu with ideally parallel TBs. Extended Data Fig. 9g shows the overlap of the ascending branches of corresponding hysteresis loops from different loading steps, suggesting a history-independent cyclic response of the tilted-TB sample.

We have considered an additional NT-Cu sample with TBs tilted at 20° relative to the loading axis. It is found that three conventional types of dislocation mechanisms, namely Hall–Petch type dislocations with Burgers vectors inclined to TBs[19,49,50], threading dislocations[17] on different slip systems blocking the motion of each other, and twinning partial dislocations gliding on TBs[20–24], are simultaneously activated under cyclic deformation (see Extended Data Fig. 9h and Supplementary Video 8), in distinct contrast to the dominance of CNDs in NT-Cu samples with TBs parallel to the loading direction.

Cyclic deformation of NT-Cu with randomly oriented TBs. Cyclic deformation behaviour of NT-Cu with randomly oriented nanotwins has also been investigated through MD simulations of a three-dimensional polycrystalline NT-Cu sample (Extended Data Fig. 9i) with dimensions of $60 \times 60 \times 60\,\mathrm{nm}^3$ and containing 27 randomly oriented grains with a mean grain size of 20 nm. Each grain further contains a set of twin planes with TB spacing of 5 nm. The total number of atoms in this sample is approximately 18 million. Periodic boundary conditions are imposed in all three directions. It is found that NT-Cu with randomly oriented TBs exhibits a history-dependent cyclic response under total strain amplitudes in the range of 1.5% to 2% (Extended Data Fig. 9j, k), in distinct contrast to history-independent cyclic response of highly oriented NT-Cu.

Characterization of CNDs in TEM under two-beam diffraction conditions. Owing to the severe confinement by nanoscale twins, the whole structure of CNDs with severely curved heads and tails is hardly observable in nanometre-thick TEM foils. However, the segments of CNDs (marked as blue solid lines in Fig. 4c) lying on the TBs are detectable in the nanometre-thick TEM foil if a two-beam diffraction technique in TEM[27] is adopted. The traditional bright/dark field TEM technique fails to work here because, under a single perfect [110] incident electron beam, the CND tails will overlap with the edge-on coherent TBs, leaving no traces of dislocations in the TEM image (Fig. 1f). Under the two-beam diffraction condition, the tails are projected as short and parallel dislocation segments (Fig. 4a).

The dislocation features in cyclically deformed NT-Cu under $\boldsymbol{g} = [\bar{1}11]_{\mathrm{M}}$ from the matrix ($[\bar{1}11]_{\mathrm{T}}$ and $[\bar{2}00]_{\mathrm{T}}$ from the twin) are similar to those in Fig. 4a under $\boldsymbol{g} = [\bar{2}00]_{\mathrm{M}}$ from the matrix. Nevertheless, these dislocation segments become invisible under $\boldsymbol{g} = [111]_{\mathrm{M/T}}$ either in matrix (M) or in adjacent twin lamellae (T). On the basis of the extinction rule of dislocations becoming visible under $\boldsymbol{g} \cdot \boldsymbol{b} = \pm 1$, where $\boldsymbol{b}$ is the Burgers vector[27,28], it is found that the Burgers vector of dislocation segments in Fig. 4a is parallel to TBs.

Data and code availability. All data generated or analysed during this study are included in this Letter and its Supplementary Information. Atomistic simulations were performed using MD code LAMMPS, which is freely available at http://lammps.sandia.gov/.

33. Agnew, S. R., Vinogradov, A. Y., Hashimoto, S. & Weertman, J. R. Overview of fatigue performance of Cu processed by severe plastic deformation. *J. Electron. Mater.* **28,** 1038–1044 (1999).
34. Höppel, H. W., Brunnbauer, M. & Mughrabi, H. in *Proceedings of Materials Week 2000* Ch. 25, 1–8 (Werkstoffwoche-Partnerschaft, 2000).
35. Abel, A. Fatigue of copper single crystals at low constant plastic strain amplitudes. *Mater. Sci. Eng.* **36,** 117–124 (1978).
36. Polák, J., Obrtlik, K. & Helesic, J. Cyclic strain localization in polycrystalline copper at room-temperature and low-temperatures. *Mater. Sci. Eng. A* **132,** 67–76 (1991).
37. Wang, R. & Mughrabi, H. Secondary cyclic hardening in fatigued copper monocrystals and polycrystals. *Mater. Sci. Eng.* **63,** 147–163 (1984).
38. Li, X. W., Wang, Z. G., Li, G. Y., Wu, S. D. & Li, S. X. Cyclic stress-strain response and surface deformation features of [011] multiple-slip-oriented copper single crystals. *Acta Mater.* **46,** 4497–4505 (1998).
39. Lepistö, T. K. & Kettunen, P. O. Comparison of the cyclic stress–strain behavior of single-and <111> multiple-slip-oriented copper single-crystals. *Mater. Sci. Eng.* **83,** 1–15 (1986).
40. Christ, H. J. & Mughrabi, H. Cyclic stress-strain response and microstructure under variable amplitude loading. *Fatigue Fract. Eng. Mater. Struct.* **19,** 335–348 (1996).
41. Morrow, J. D. in *Internal Friction, Damping, and Cyclic Plasticity* (ed. Lazan, B. J.) 45–87 (Special Technical Publication 378, American Society for Testing of Materials, 1965).
42. Nosé, S. A unified formation of the constant temperature molecular-dynamic methods. *J. Chem. Phys.* **81,** 511–519 (1984).

43. Hoover, W. G. Constant-pressure equations of motion. *Phys. Rev. A* **34,** 2499–2500 (1986).
44. Mishin, Y., Mehl, M. J., Papaconstantopoulos, D. A., Voter, A. F. & Kress, J. D. Structural stability and lattice defects in copper: ab initio, tight-binding, and embedded-atom calculations. *Phys. Rev. B* **63,** 224106 (2001).
45. Li, X. Y., Wei, Y. J., Lu, L., Lu, K. & Gao, H. J. Dislocation nucleation governed softening and maximum strength in nano-twinned metals. *Nature* **464,** 877–880 (2010).
46. Faken, D. & Jonsson, H. Systematic analysis of local atomic structure combined with 3D computer graphics. *Comput. Mater. Sci.* **2,** 279–286 (1994).
47. Zhou, H. F. & Gao, H. J. A plastic deformation mechanism by necklace dislocations near crack-like defects in nanotwinned metals. *J. Appl. Mech.* **82,** 071015 (2015).
48. Zhu, Y. X., Li, Z. H., Huang, M. S. & Liu, Y. Strengthening mechanisms of the nanolayered polycrystalline metallic multilayers assisted by twins. *Int. J. Plast.* **72,** 168–184 (2015).
49. Chowdhury, P. B., Sehitoglu, H. & Rateick, R. G. Predicting fatigue resistance of nano-twinned materials: Part I. Role of cyclic slip irreversibility and Peierls stress. *Int. J. Fatigue* **68,** 277–291 (2014).
50. Lu, K. Stabilizing nanostructures in metals using grain and twin boundary architectures. *Nat. Rev. Mater.* **1,** 16019 (2016).

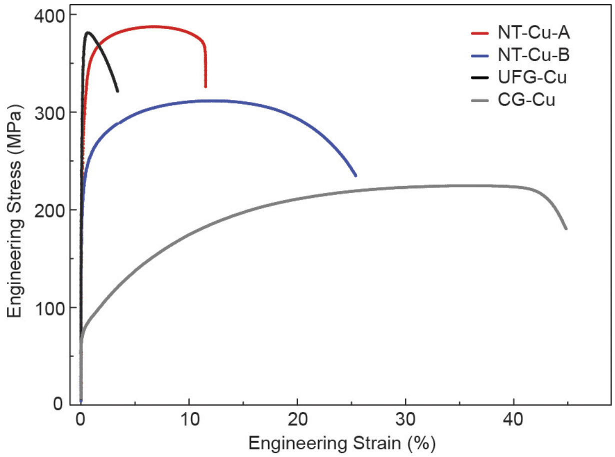

Extended Data Figure 1 | Engineering stress–strain curves of NT-Cu, UFG-Cu and CG-Cu samples in uniaxial tensile experiments. At least three repeated tensile tests were performed on each sample.

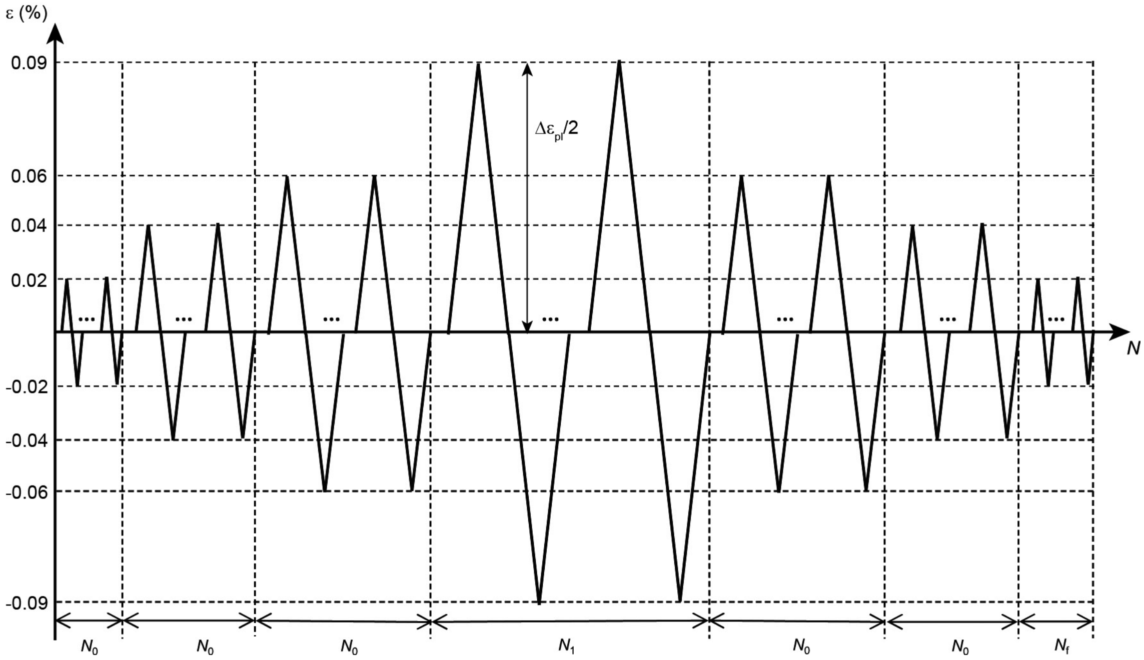

Extended Data Figure 2 | Long-cycle symmetric tension–compression loading procedure imposed on NT-Cu samples. Under strain control, a triangular wave loading profile was used. The applied plastic strain amplitude $\Delta\varepsilon_{pl}/2$ increases stepwise from 0.02% to 0.04%, 0.06% and 0.09%, and then decreases back to 0.02%. $N_0 = 1{,}500$ cycles, $N_1 = 500$ cycles and N_f is the number of cycles up to final failure.

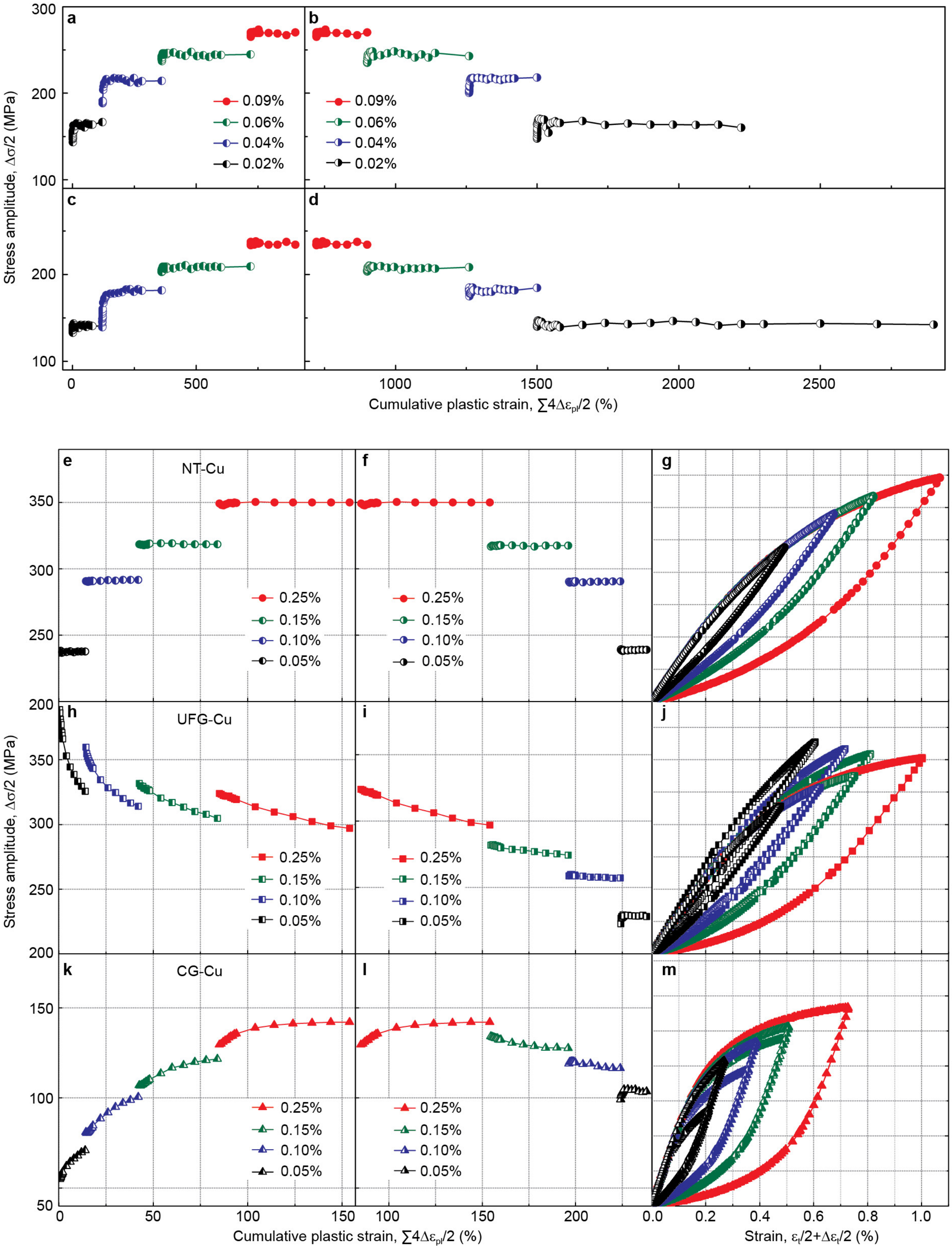

Extended Data Figure 3 | History-independent cyclic response of NT-Cu. Cyclic stress response as a function of the cumulative plastic strain for NT-Cu-A (**a**, **b**) and NT-Cu-B (**c**, **d**) cyclically deformed by increasing $\Delta\varepsilon_{pl}/2$ step-by-step from 0.02% to 0.09% and decreasing back to 0.02%. Cyclic stress response of NT-Cu-A (**e**, **f**), UFG-Cu (**h**, **i**) and CG-Cu (**k**, **l**) cyclically deformed by increasing $\Delta\varepsilon_{pl}/2$ step-by-step from 0.05% to 0.25% and decreasing back to 0.05%, with cyclic numbers of 70 at each $\Delta\varepsilon_{pl}/2$. Their corresponding hysteresis loops (at the 50th cycle of each $\Delta\varepsilon_{pl}/2$) are shown in **g**, **j** and **m**, respectively.

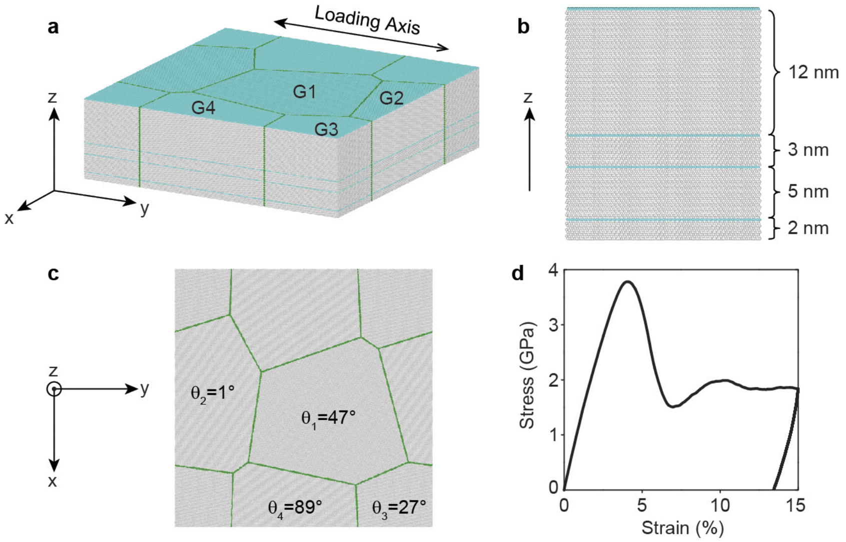

Extended Data Figure 4 | Atomistic simulation setup. a, Perspective view of the initial configuration of NT-Cu. **b**, Cross sectional view of a typical NT grain G4. Each grain in **a** has the same TB distribution. **c**, View of the NT-Cu sample in *x*–*y* projection. The misorientation angle θ_i ($i = 1, 2, 3$ and 4) of the *i*th grain represents the angle between its [110] direction and the *y* axis. Colours are assigned to atoms according to their local crystal structure. **d**, Simulated tensile loading and unloading stress–strain curves of NT-Cu.

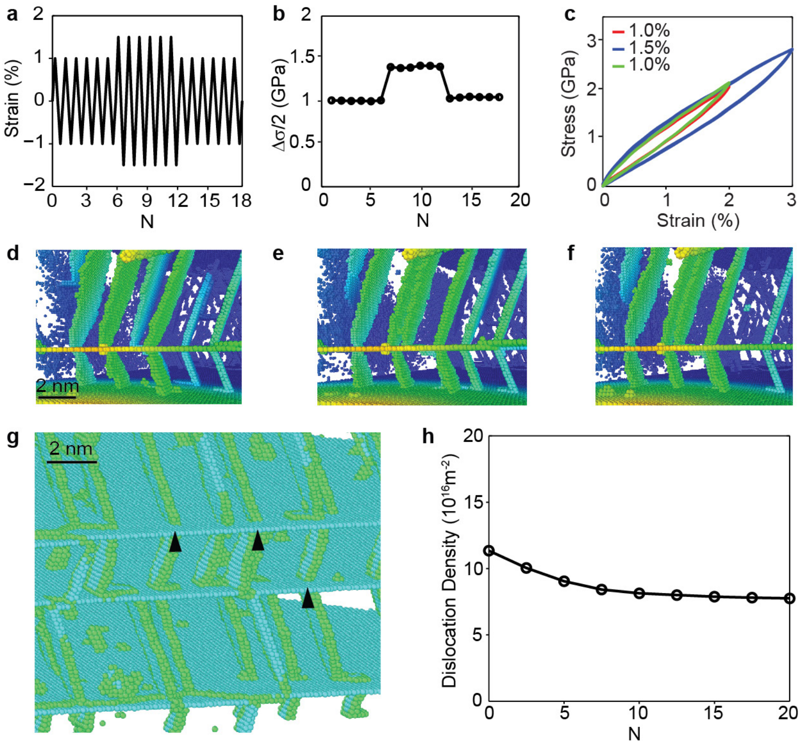

Extended Data Figure 5 | History-independent cyclic response of NT-Cu demonstrated by MD simulations. a, Three-step cyclic loading scheme. **b**, **c**, Simulated $\Delta\sigma/2$ versus N relation and hysteresis loops. **d**–**f**, Snapshots of NT-Cu captured at three sequential cycles (that is, $N = 1$, 10 and 20) at $\Delta\varepsilon_t/2 = 1\%$ (corresponding to $\Delta\varepsilon_{pl}/2 = 0.25\%$). Colours are assigned to atoms based on their spatial coordinates. **g**, CNDs formed by tail-linkage or TB transmission (indicated by black arrows) during cyclic loading. See Extended Data Fig. 7 for details on the formation mechanism of CNDs. Colours are assigned to atoms based on their local crystal structure. **h**, The dislocation density reaches a plateau after ten cycles at $\Delta\varepsilon_t/2 = 1\%$.

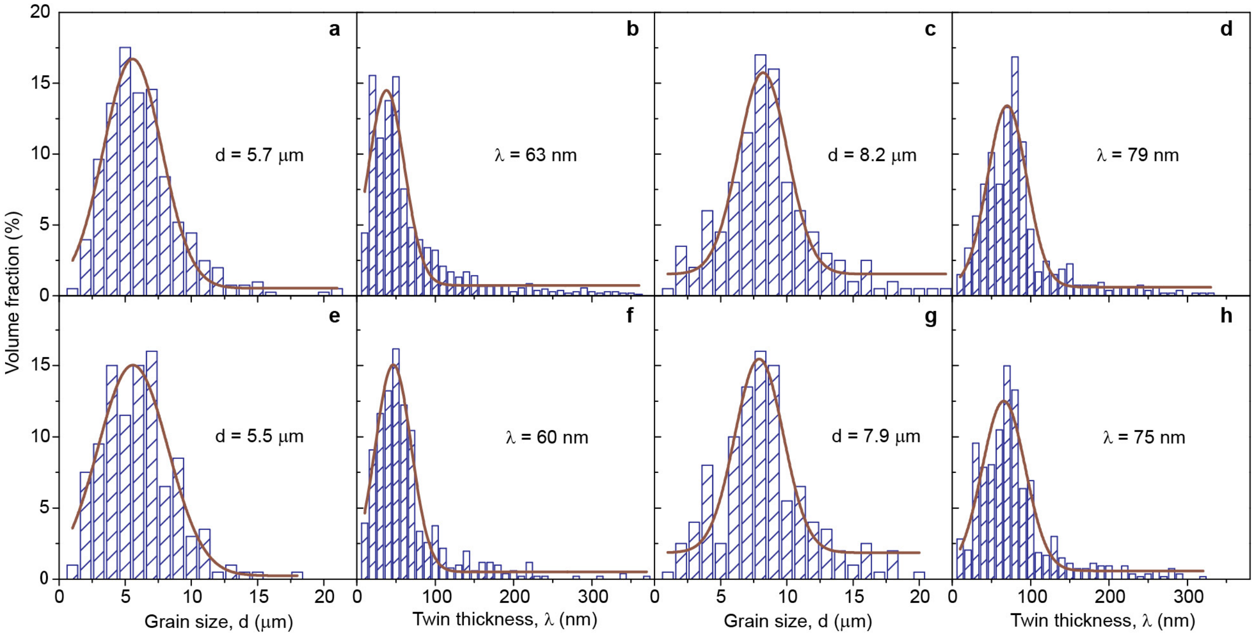

Extended Data Figure 6 | Stability of NT structure under cyclic deformation. The grain size (**a**, **c**, **e**, **g**) and twin thickness (**b**, **d**, **f**, **h**) distributions of both NT-Cu-A and NT-Cu–B samples before (**a**–**d**) and after being cyclically deformed to failure (**e**–**h**), showing no detectable changes in the mean grain size and twin thickness between the as-deposited and cyclically deformed states. In each panel, the value given for *d* or λ is the mean of the values plotted.

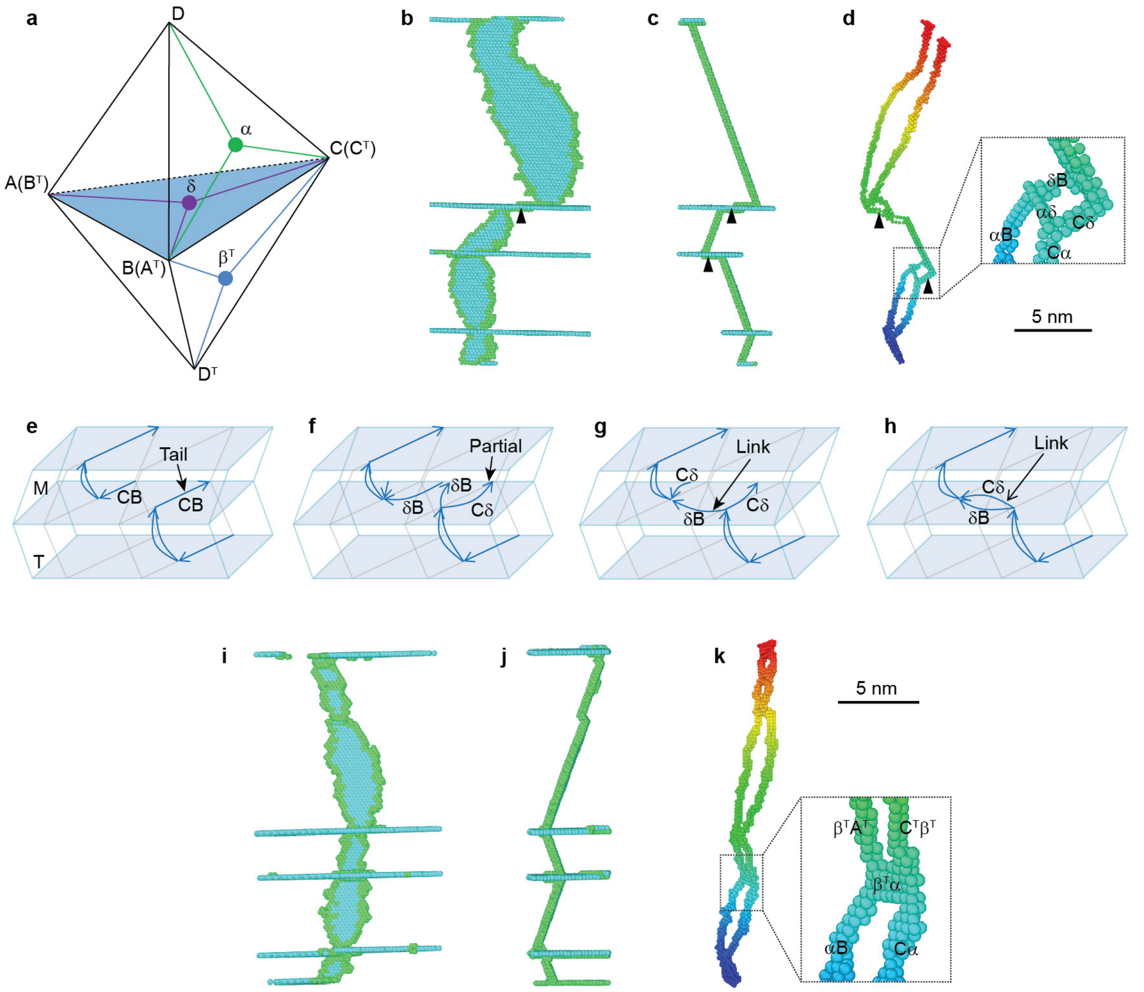

Extended Data Figure 7 | Formation mechanism of CNDs in NT-Cu under cyclic loading. a, Double Thompson tetrahedron representation of the slip systems in matrix (upper) and twin (lower). **b**, **c**, Atomic configurations of a typical CND projected along the $[\bar{1}2\bar{1}]$ and $[\bar{1}01]$ crystallographic directions. Atoms in fcc structure are made transparent for clarity. **d**, Perspective view of the same CND with hcp atoms hidden to emphasize the necklace-like feature of the dislocation. The inset shows the Burgers vectors of an extended stair-rod component of a CND which bends from the matrix to the twin plane. **e**–**h**, Schematics showing the formation of CNDs through the linking of threading dislocation tails in adjacent twin layers under cyclic loading. **i**–**k**, Sometimes threading tails can also slip across TBs.

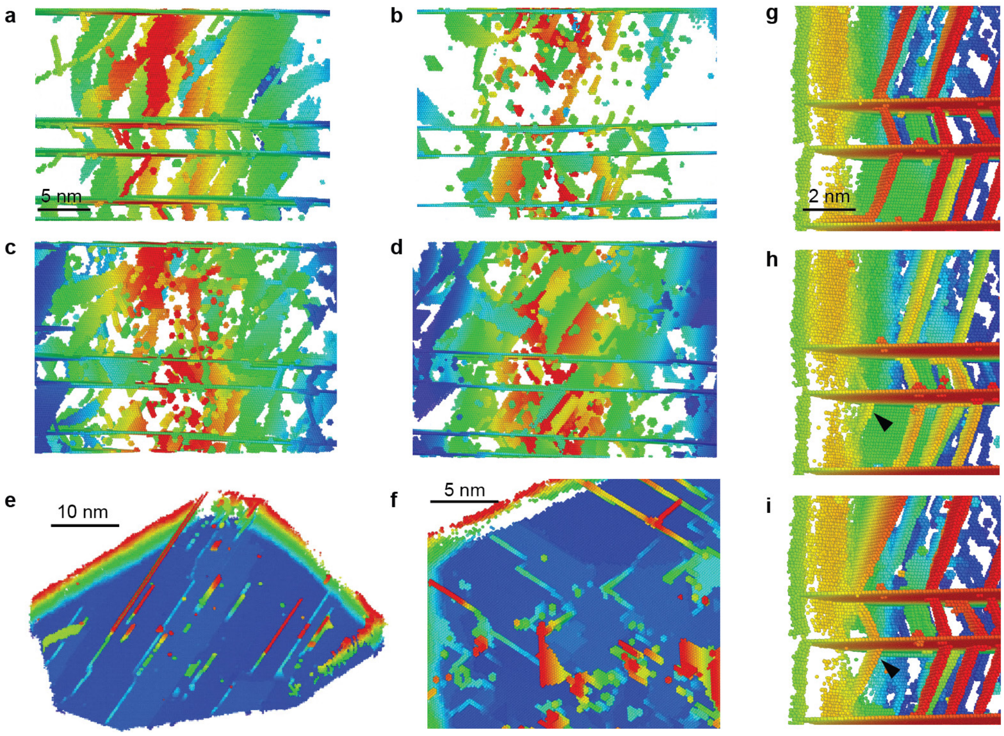

Extended Data Figure 8 | Deformation patterns in grains labelled as G1–G4 in Extended Data Fig. 4 after 20 tension–compression cycles with $\Delta\varepsilon_t/2 = 1\%$. a–d, A single slip system is activated in G1 (**a**), whereas double slip systems are activated in G2–G4 (**b–d**) during cyclic deformation. **e**, Parallel slip traces observed in G1. **f**, Numerous dislocation locks are observed in G4. **g–i**, Snapshots showing a typical CND (indicated by black arrows) emerging from a grain boundary as a single unit in cyclically deformed NT-Cu sample (see details in Methods). Colours are assigned to atoms based on their spatial coordinates.

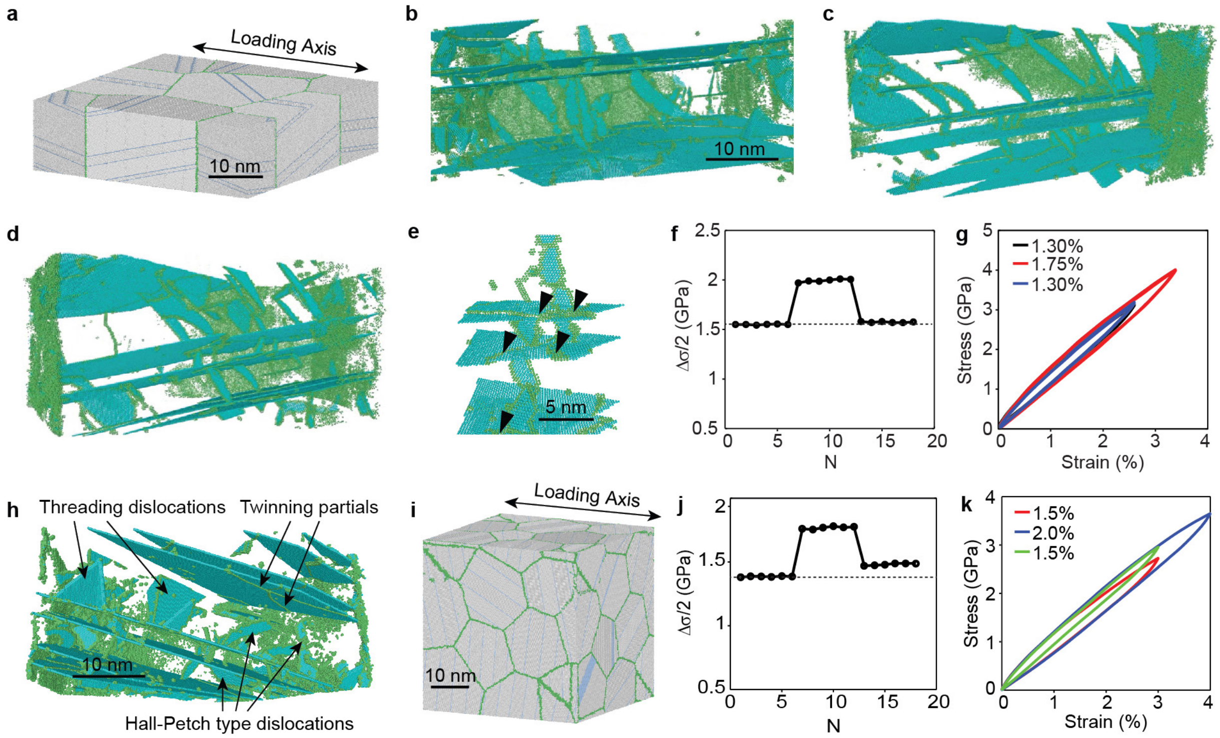

Extended Data Figure 9 | Molecular dynamics simulations showing history-independent cyclic response of NT-Cu containing tilted TBs with respect to the loading axis. a, NT-Cu containing tilted TBs with respect to the loading axis. **b**–**d**, CNDs in NT-Cu samples with tilt angles of 5° (**b**), 10° (**c**) and 15° (**d**) under cyclic loading, respectively. **e**, Typical CND structure observed in tilted TBs. CND tails connecting threading segments in neighbouring twin layers are indicated by black arrows. **f**, Relationship $\Delta\sigma/2$ and N for tilt angle of 15°; **g**, the corresponding hysteresis loops. **h**, Cyclic deformation of NT-Cu with TBs tilted 20° with respect to the loading axis is governed by the three types of dislocation mechanism shown. **i**, Simulated NT-Cu sample containing 27 grains with randomly oriented TBs. **j**, Relationship between $\Delta\sigma/2$ and N demonstrating history-dependent cyclic response of randomly oriented NT sample. **k**, The corresponding hysteresis loops for different $\Delta\varepsilon_t/2$.

Extended Data Table 1 | Activated slip systems in NT-Cu during the cyclic experiments illustrated with double Thompson tetrahedron

Slip system	Slip plane	Slip direction	$\boldsymbol{g}_M \cdot \boldsymbol{b}$		
			$\boldsymbol{g}_M$ $[\bar{1}11]$	$[\bar{2}00]$	$[111]$
$(11\bar{1})[\bar{1}10]$	DAB	AB	1	1	0
$(\bar{1}11)[01\bar{1}]$	DAC	AC	0	0	0
$(1\bar{1}1)[\bar{1}01]$	DBC	BC	1	1	0

Three different diffraction ***g*** vectors from the matrix are used in two-beam diffraction images of dislocations: $\boldsymbol{g} \cdot \boldsymbol{b} = 1$ corresponds to visible dislocations and $\boldsymbol{g} \cdot \boldsymbol{b} = 0$ corresponds to invisible dislocations, based on the dislocation extinction rule. Dislocations with slip plane inclined to TBs but slip direction parallel to TBs are visible in the matrix under $\boldsymbol{g} = [\bar{1}11]_M$ and $[\bar{2}00]_M$ but invisible under $\boldsymbol{g} = [111]_M$. A similar rule applies to visible dislocations in twins under the corresponding $\boldsymbol{g}_T$.